

# Distance Velocity–Azimuth Display (DVAD)—New Interpretation and Analysis of Doppler Velocity

WEN-CHAU LEE

*National Center for Atmospheric Research,\* Boulder, Colorado*

XIAOWEN TANG

*Key Laboratory for Mesoscale Severe Weather/MOE and School of Atmospheric Sciences, Nanjing University, Nanjing, China*

BEN J.-D. JOU

*Department of Atmospheric Sciences, National Taiwan University, Taipei, Taiwan*

(Manuscript received 9 June 2013, in final form 1 October 2013)

## ABSTRACT

The concept and mathematical framework of the distance velocity–azimuth display (DVAD) methodology is presented. DVAD uses  $rV_d$  (Doppler velocity scaled by the distance from the radar to a gate,  $r$ ) as the basis to display, interpret, and extract information from single Doppler radar observations. Both linear and nonlinear wind fields can be represented by the same Cartesian polynomial with different orders. DVAD is mathematically concise and superior to the velocity–azimuth display (VAD) in interpreting and deducing flow characteristics. The  $rV_d$  pattern of a two-dimensional linear wind field is exclusively in the form of a bivariate quadratic equation representing conic sections (e.g., ellipse, parabola, and hyperbola) centered at the radar depending only on divergence and deformation. The presence of a constant background flow translates the conic sections to a different origin away from the radar. It is possible to graphically estimate the characteristics of a linear wind field from the conical sections without performing a VAD analysis. DVAD analysis can deduce quantitative flow characteristics by a least squares fitting and/or a derivative method, and is a natural way to account for nonlinearity. The  $rV_d$  pattern behaves similar to a type of velocity potential in fluid mechanics where  $\nabla(rV_d)$  is a proxy of the true wind vector and is used to estimate the general flow pattern in the vicinity of the radar.

## 1. Introduction

Since the invention of weather Doppler radar, the Doppler velocity  $V_d$  displayed in a plan position indicator (PPI) or a range–height indicator (RHI) are commonly used to interpret the wind flow structure of meteorological phenomena in both operations and research. Doppler velocity is the projection of the three-dimensional (3D)

target motion along the radar beam direction. As a result, the full 3D air motion cannot be measured directly and can only be deduced if there are simultaneous observations from two or more Doppler radars on the same target plus application of the continuity equation (e.g., Armijo 1969). Otherwise, only characteristics of certain simple meteorological flow patterns, for example, straight-line wind, rotational wind, and converging/diverging wind, can be qualitatively identified via their Doppler velocity patterns (e.g., Lhermitte and Atlas 1961; Donaldson 1970; Wood and Brown 1992). Quantitative description of the wind structures of the aforementioned specific flow patterns and their derived quantities (e.g., convergence, deformation, and/or vorticity) can be estimated by single-Doppler wind retrieval algorithms such as the velocity–azimuth display (VAD);

\*The National Center for Atmospheric Research is sponsored by the National Science Foundation.

*Corresponding author address:* Dr. Wen-Chau Lee, National Center for Atmospheric Research, 3450 Mitchell Ln., Boulder, CO 80303.  
E-mail: wenchau@ucar.edu

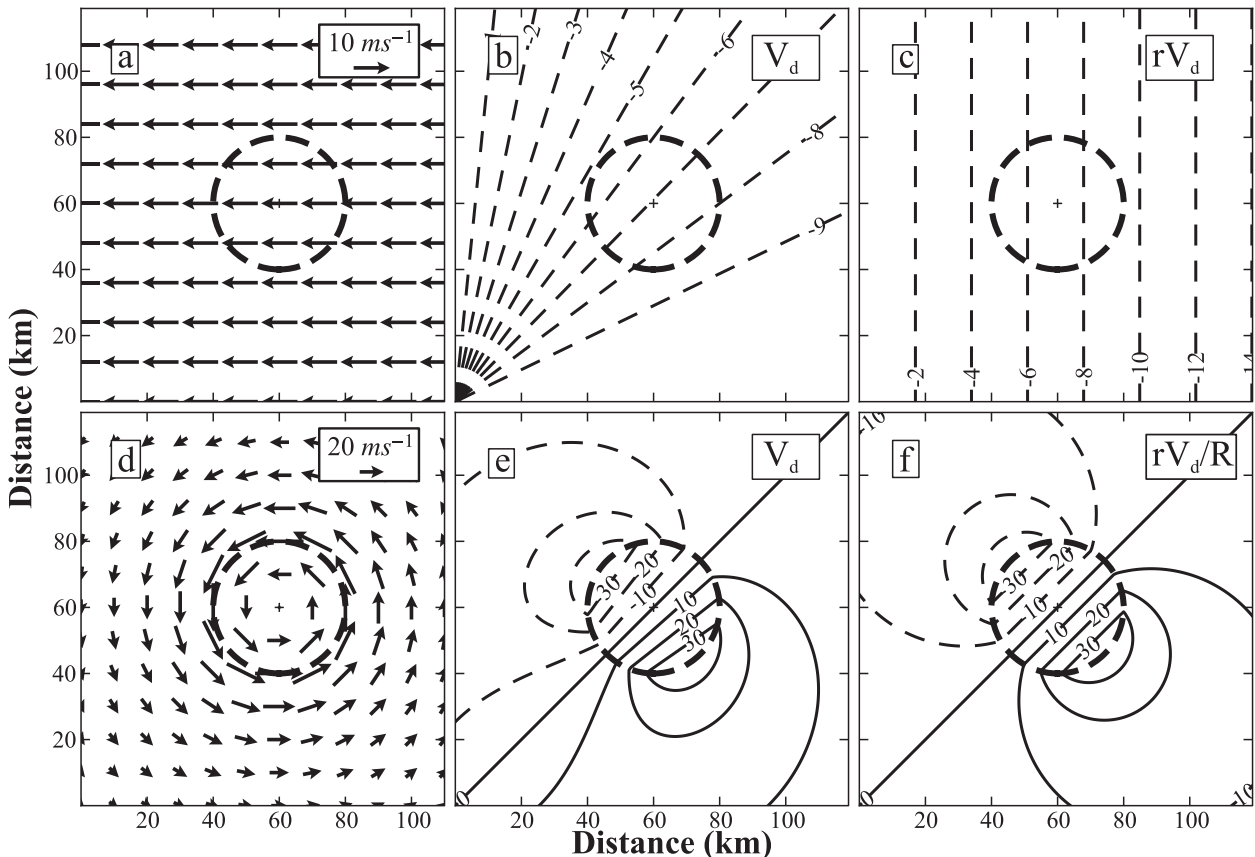


FIG. 1. (a) The flow field of a constant easterly wind; (b) the Doppler velocity,  $V_d$ , of the wind field in (a) sampled by a Doppler radar located at (0, 0), the bottom-left corner; (c) the corresponding  $rV_d$  display of the same background flow; (d) the flow field of a Rankine-combined vortex; (e)  $V_d$  as in (b), but for the vortex in (d); and (f)  $rV_d/R$  as in (c), but for the vortex in (d), where  $R$  is the distance from the Doppler radar to the vortex center. The units of  $V_d$ ,  $rV_d$ , and  $rV_d/R$  are  $\text{m s}^{-1}$ ,  $\text{m}^2 \text{s}^{-1}$ , and  $\text{m s}^{-1}$ , respectively.

Browning and Wexler 1968; Caya and Zawadzki 1992; Donaldson 1991; Matejka and Srivastava 1991), volume velocity processing (VVP; Waldeufel and Corbin 1979; Koscielny et al. 1982; Boccippio 1995), and velocity track display (e.g., VTD; Lee et al. 1994; Roux and Marks 1996; Lee et al. 1999). Although these algorithms use the same PPI or constant altitude PPI (CAPPI) data, the underlying flow models are either centered at the radar (e.g., VAD) or at a user-selected location (e.g., VVP and VTD).

While manipulating the Doppler velocity equation to formulate the generalized VTD (GVTD) technique, Jou et al. (2008) showed that the atmospheric vortex signatures displayed in  $rV_d$  ( $V_d$  scaled by the distance from the radar to the gate,  $r$ ) had several advantages over those displayed in  $V_d$  and simplified the governing equations. First, the signature of a constant wind (Fig. 1a) possesses a set of parallel lines (Fig. 1c) compared to a starburst pattern displayed in  $V_d$  (Fig. 1b). It has been shown in Jou et al. (2008) that the gradient of these parallel lines of  $rV_d$  is the constant wind vector. Second, the  $V_d$  pattern of an axisymmetric atmospheric vortex

(Fig. 1d) possesses geometric distortion due to the scanning characteristics of a ground-based Doppler radar; for example, the Doppler velocity dipole is skewed toward the radar as a function of the distance from the radar to the vortex center accompanied by nonparallel constant  $V_d$  lines inside the radius of maximum wind (RMW; the dashed circle in Fig. 1e). The aforementioned geometric distortion for an axisymmetric vortex is no longer a factor displayed in  $rV_d/R$  (i.e., Fig. 1f), where  $R$  is the distance between the radar and the vortex center. Further examining of the properties of  $rV_d$  suggests that  $rV_d$  can be expressed in a Cartesian coordinate and have a wider application beyond atmospheric vortices documented in Jou et al. (2008).

The use of  $rV_d$  and its accompanied polynomial form in the Cartesian coordinate to represent linear and non-linear wind fields were first presented in Peace et al. (1969). These authors demonstrated that a convective cell moving in space observed by a Doppler radar at two different times is equivalent to observing the same cell with two Doppler radars from two vantage points, if storm

evolution can be ignored. Therefore, the 2D horizontal wind fields within a convective cell can be deduced using two different volumes of data from the same radar. This methodology was later termed “synthetic dual-Doppler analysis” (e.g., Bluestein and Hazen 1989; Bluestein et al. 1994). When the wind field is stationary in the moving frame, Gal-Chen (1982) recognized that the second derivative of  $rV_d$  with respect to time is invariant. Hence,  $rV_d$  can be used to determine the optimal advection speed of an atmospheric phenomenon. These authors recognized the potential advantages in working with  $rV_d$  but they did not focus on its single-Doppler radar applications.

One of main difficulties of utilizing the single-Doppler radial velocity information in interpreting flow patterns is its vectorlike property that lacks a general relationship to the corresponding 3D Cartesian wind vectors. The purpose of this paper is to revisit this nearly forgotten quantity,  $rV_d$ , and illustrate the advantages of using  $rV_d$  as a new framework to display, examine, and interpret single-Doppler velocities on linear and nonlinear atmospheric flow patterns beyond those documented in Peace et al. (1969) and Gal-Chen (1982). It will be shown that the polynomial representation of  $rV_d$  of linear wind fields is mathematically equivalent to the VAD. Therefore, qualitative information of a linear wind field can be deduced by a 2D least squares fit of  $rV_d$ . Since the  $rV_d$  display of a linear wind field is a quadratic curve, the linear terms except for the vorticity can be graphically estimated from the shape, contour values, and orientation of the corresponding quadratic curve without actually performing a series of VAD analyses. In the presence of nonlinear wind components,  $rV_d$  has a more concise mathematical representation over the nonlinear VAD analysis (e.g., Caya and Zawadzki 1992) in deducing kinematic properties. Because of the mathematical similarity to the VAD, the proposed methodology is coined distance velocity–azimuthal display (DVAD).

This paper is organized as follows. Section 2 presents the rationale and the mathematic framework of the DVAD. Section 3 illustrates characteristics of DVAD on several simple, analytical flow fields. Section 4 demonstrates how to quantitatively deduce flow characteristics

via least squares fitting and taking straight derivatives of the  $rV_d$  field. Graphical interpretation of a real wind field using DVAD is illustrated in section 5. Summary and future work are presented in section 6.

## 2. The DVAD methodology

### a. Mathematic expression and properties of DVAD

For a radar located at the origin, the Doppler velocity  $V_d$  at any point  $P(x, y, z)$  in space can be expressed in terms of the three-dimensional Cartesian velocities,  $u$ ,  $v$ , and,  $w$ , and the spherical coordinate parameters: mathematic angle  $\theta$  (defined as  $0^\circ$  pointing east and increasing positively counterclockwise), elevation angle  $\phi$ , and range  $r$ , from the radar to each gate, as illustrated in Armijo (1969):

$$\begin{aligned} r &= (x^2 + y^2 + z^2)^{1/2} \\ \theta &= \tan^{-1} \frac{y}{x} \\ \phi &= \sin^{-1} \frac{z}{r} \\ V_d &= u \cos \theta \cos \phi + v \sin \theta \cos \phi + w \sin \phi \\ &= u \frac{x}{r} + v \frac{y}{r} + w \frac{z}{r}. \end{aligned}$$

Hence, by multiplying  $r$  on both sides, we obtain the following:

$$rV_d = ux + vy + wz. \quad (1)$$

Here we ignore the contribution from the terminal fall velocity of the particle, as well as the effects of atmospheric refraction and earth curvature on radar beam height. The characteristics between  $rV_d$  and  $V_d$  differ in many aspects. First, by examining Eq. (1),  $rV_d$  can be expressed exactly by Cartesian coordinate quantities while  $V_d$  involves a spherical coordinate quantity  $r$ . In general, coordinate transformation changes the form of the expressions but will not add more information. This point will be illustrated in section 2b. Second, taking the gradient of Eq. (1), we obtain the following:

$$\begin{aligned} \nabla(rV_d) &= (u + xu_x + yv_x + zw_x)\mathbf{i} + (v + xu_y + yv_y + zw_y)\mathbf{j} + (w + xu_z + yv_z + zw_z)\mathbf{k} \\ &= \mathbf{V} + (xu_x + yv_x + zw_x)\mathbf{i} + (xu_y + yv_y + zw_y)\mathbf{j} + (xu_z + yv_z + zw_z)\mathbf{k}, \end{aligned} \quad (2)$$

where  $\mathbf{V} = u\mathbf{i} + v\mathbf{j} + w\mathbf{k}$  is the 3D Cartesian velocity vector of a target at point  $P$ . As a result,  $rV_d$  possesses a property similar to a type of velocity potential (a scalar) in fluid mechanics where its gradient is the three-dimensional

velocity vector  $\mathbf{V}$ , plus the first derivative of  $u$ ,  $v$ , and  $w$  scaled by their corresponding Cartesian distance  $x$ ,  $y$ , and  $z$ . In contrast,  $V_d$  behaves like a vector and does not possess similar mathematic and physical characteristics

as  $rV_d$ . These first-order derivative terms in Eq. (2) prevent the direct computation of the velocity vector  $\mathbf{V}$  other than at the origin (i.e., the radar). When the last three terms on the right-hand side of Eq. (2) are small,  $\nabla(rV_d)$  is a proxy of the 3D velocity vector  $\mathbf{V}$ . However, without the knowledge of the spatial gradient of the velocity field, the use of “ $\nabla(rV_d)$  as a proxy of the 3D velocity vector  $\mathbf{V}$ ” is mostly valid in a region close to the radar.

### b. Expressions of DVAD for linear and nonlinear wind fields

To investigate the properties of DVAD of linear and nonlinear wind fields,  $u$ ,  $v$ , and  $w$  in Eq. (1) can be expanded in Taylor series with respect to the origin  $(x_0, y_0, z_0)$  in space, then Eq. (1) will take a form of trivariate polynomial as follows:

$$\begin{aligned}
 rV_d(x_0 + \Delta x, y_0 + \Delta y, z_0 + \Delta z) &= u \times (x_0 + \Delta x) + v \times (y_0 + \Delta y) + w \times (z_0 + \Delta z) \\
 &= u_0 x_0 + v_0 y_0 + w_0 z_0 + u_0 \Delta x + v_0 \Delta y + w_0 \Delta z + u_x x_0 \Delta x + u_x (\Delta x)^2 \\
 &\quad + u_y x_0 \Delta y + u_y \Delta x \Delta y + u_z x_0 \Delta z + u_z \Delta x \Delta z + v_x x_0 \Delta x + v_x (\Delta x)^2 \\
 &\quad + v_y y_0 \Delta y + v_z \Delta y \Delta z + v_z y_0 \Delta z + w_x x_0 \Delta x + w_x \Delta x \Delta z + w_y z_0 \Delta y + w_y \Delta y \Delta z \\
 &\quad + \frac{1}{2} [u_{xx} x_0 (\Delta x)^2 + u_{xx} (\Delta x)^3 + u_{yy} x_0 (\Delta y)^2 + u_{yy} \Delta x (\Delta y)^2 + u_{zz} x_0 (\Delta z)^2 + u_{zz} \Delta x (\Delta z)^2] \\
 &\quad + [u_{xy} x_0 \Delta x \Delta y + u_{xy} (\Delta x)^2 \Delta y + u_{xz} x_0 \Delta x \Delta z + u_{xz} (\Delta x)^2 \Delta z + u_{yz} x_0 \Delta y \Delta z + u_{xy} \Delta x \Delta y \Delta z] \\
 &\quad + \frac{1}{2} [v_{xx} y_0 (\Delta x)^2 + v_{xx} (\Delta x)^2 \Delta y + v_{yy} y_0 (\Delta y)^2 + v_{yy} (\Delta y)^3 + v_{zz} y_0 (\Delta z)^2 + v_{zz} \Delta y (\Delta z)^2] \\
 &\quad + [v_{xy} y_0 \Delta x \Delta y + v_{xy} (\Delta y)^2 \Delta x + v_{xz} y_0 \Delta x \Delta z + v_{xz} \Delta x \Delta y \Delta z + v_{yz} y_0 \Delta y \Delta z + v_{xy} (\Delta y)^2 \Delta z] \\
 &\quad + \frac{1}{2} [w_{xx} z_0 (\Delta x)^2 + w_{xx} (\Delta x)^2 \Delta z + w_{yy} z_0 (\Delta y)^2 + w_{yy} (\Delta y)^2 \Delta z + w_{zz} z_0 (\Delta z)^2 + w_{zz} (\Delta z)^3] \\
 &\quad + [w_{xy} z_0 \Delta x \Delta y + w_{xy} \Delta x \Delta y \Delta z + w_{xz} z_0 \Delta x \Delta z + w_{xz} \Delta x (\Delta z)^2 + w_{yz} z_0 \Delta y \Delta z + w_{xy} (\Delta z)^2 \Delta y] + \dots, \quad (3)
 \end{aligned}$$

where  $u_0$ ,  $v_0$ , and  $w_0$  are the three-dimensional velocities at the point  $(x_0, y_0, z_0)$ . The right-hand side of Eq. (3) is a polynomial expressed in a Cartesian coordinate system and its highest order is one above the highest order of the underlying linear or nonlinear flow fields. Although the Taylor series can be expanded with respect to any point other than the radar at the origin, there are no advantages because Eq. (3) becomes unnecessarily complicated and the full wind field still cannot be deduced other than at the radar [e.g., Eq. (2)] as presented in many previous single-Doppler radar wind retrieval works (e.g., Browning and Wexler 1968; Peace et al. 1969; Waldteufel and Corbin 1979; Koscielny et al. 1982). Therefore, Eq. (3) can be simplified when expanding the Taylor series with respect to the radar (i.e.,  $x_0 = y_0 = z_0 = 0$ ). For the convenience of illustration, we will focus on the 2D form of Eq. (3) by setting  $\Delta z = 0$  and  $\Delta x$  and  $\Delta y$  become  $x$  and  $y$ . Then Eq. (3) becomes

$$\begin{aligned}
 rV_d &= u_0 x + v_0 y + u_x x^2 + (u_y + v_x)xy + v_y y^2 \\
 &\quad + \frac{1}{2} [u_{xx} x^3 + (u_{xx} + 2u_{xy})x^2 y + (u_{yy} + 2v_{xy})xy^2 \\
 &\quad + v_{yy} y^3] + \dots, \quad (4)
 \end{aligned}$$

where Eq. (4) is in a form of a standard polynomial where the coefficient of each term is a combination of physical quantities of a given wind field.<sup>1</sup> Note that Eq. (4) should be processed on CAPPI data. Since the geometric characteristics of polynomials are easy to recognize visually (especially for the first- and second-order polynomials), displaying and processing  $rV_d$  rather than  $V_d$  make the subsequent interpretation and computation of the gross wind field properties much more intuitive.

### c. Characteristics of DVAD for linear, nonrotational wind fields

When considering only linear wind fields, the second-order derivatives are zero and Eq. (4) reduces to a bivariate quadratic equation (e.g., Korn and Korn 1961, 39–41):

<sup>1</sup> Note that Eq. (4) recovers Eq. (9) in Peace et al. (1969) when the distance to radar  $R_0$  equals 0.

$$0 = u_0x + v_0y + u_x x^2 + (u_y + v_x)xy + v_y y^2 - rV_d = u_x x^2 + (u_y + v_x)xy + v_y y^2 + u_0x + v_0y - rV_d \\ = u_x(x - x_0)^2 + (u_y + v_x)(x - x_0)(y - y_0) + v_y(y - y_0)^2 + F, \quad (5)$$

where

$$F = \begin{vmatrix} u_x & (u_y + v_x)/2 & u_0/2 \\ (u_y + v_x)/2 & v_y & v_0/2 \\ u_0/2 & v_0/2 & -rV_d \end{vmatrix} \bigg/ \begin{vmatrix} u_x & (u_y + v_x)/2 \\ (u_y + v_x)/2 & v_y \end{vmatrix}.$$

Equation (5) is a bivariate quadratic equation, representing conic sections.<sup>2</sup> Different linear wind fields [i.e., combinations of  $u_x$ ,  $(u_y + v_x)$ ,  $v_y$ ,  $u_0$ , and  $v_0$  in Eq. (5)] yield different types of conic sections, including three types of nondegenerate quadratic curves (i.e., ellipse, parabola, and hyperbola). The geometric property of the quadratic equation is determined by the sign of the discriminant,  $\delta = (u_y + v_x)^2/4 - u_x v_y$  for Eq. (5), as follows (e.g., Taylor 1959, 297–298):

- 1)  $\delta < 0$ , a set of ellipse [If  $u_x = v_y \neq 0$  and  $u_y + v_x = 0$ , Eq. (11) represents a circle, which is a special case of ellipse];
- 2)  $\delta = 0$ , a set of parabola;
- 3)  $\delta > 0$ , a set of hyperbola.

Physically,  $\delta$  involves the square of shearing deformation and the product of two components of the divergence.

Because the square of shearing deformation is always greater or equal to zero, the only case that  $rV_d$  pattern holds an ellipse is for  $u_x v_y > (u_y + v_x)^2/4$ , which implies  $u_x v_y > 0$  is a necessary but not a sufficient condition. Therefore, a given linear wind field ( $u_x$ ,  $v_y$ ,  $u_y$ , and  $v_x$ ) yields a  $rV_d$  pattern governed by Eq. (5). Meteorologically, divergence, stretching deformation, and shearing deformation, control the  $rV_d$  pattern. However, a given  $rV_d$  pattern is only unique to  $u_x$ ,  $v_y$ , and  $(u_y + v_x)$  while the vorticity ( $v_x - u_y$ ) cannot be resolved. When the wind field is linear, DVAD and VAD are mathematically identical where the mean wind, divergence, and deformation can be deduced.

The geometric properties of the  $rV_d$  patterns for linear wind fields can be further examined via Eq. (5). The presence of a mean wind ( $u_0$ ,  $v_0$ ) is equivalent to translating the  $rV_d$  conic sections to a new origin ( $x_0$ ,  $y_0$ ) as follows (e.g., Korn and Korn 1961, 39–41):

$$x_0 = \frac{4}{[(u_y + v_x)^2 - 4u_x v_y]} \begin{vmatrix} \frac{1}{2}u_0 & \frac{1}{2}(u_y + v_x) \\ \frac{1}{2}v_0 & v_y \end{vmatrix} = \frac{[2u_0 v_y + (u_y + v_x)v_0]}{[(u_y + v_x)^2 - 4u_x v_y]} \quad (6)$$

$$y_0 = \frac{4}{[(u_y + v_x)^2 - 4u_x v_y]} \begin{vmatrix} u_x & \frac{1}{2}u_0 \\ \frac{1}{2}(u_y + v_x) & \frac{1}{2}v_0 \end{vmatrix} = \frac{[2u_x v_0 - (u_y + v_x)u_0]}{[(u_y + v_x)^2 - 4u_x v_y]}. \quad (7)$$

The magnitude and sign (i.e., direction) of the  $rV_d$  pattern translation depend on the values of the  $u_0$  and  $v_0$  and the linear wind field specified in Eqs. (6) and (7). In the VAD framework, the analysis is performed on rings centered at the radar. Hence, the linear wind fields have their centers<sup>3</sup> at the radar (see Fig. 2 in Browning

and Wexler 1968) and  $u_0$  and  $v_0$  are interpreted as “translation speed.”

Geometrically, Eq. (5) represents a general form of conic sections with an arbitrary orientation [if  $(u_y + v_x) \neq 0$ ] that can be rotated to realign the primary axes with the  $x$  and the  $y$  axes. Mathematically, this is equivalent to performing a coordinate transformation by rotating a positive acute angle  $\alpha$  as follows (e.g., Taylor 1959, 294–297):

$$\alpha = \frac{1}{2} \tan^{-1} \frac{u_y + v_x}{u_x - v_y} \quad (8)$$

and Eq. (5) can be reduced to the following form:

<sup>2</sup> Conic sections correspond to the curves which can be created by the intersection of a plane with a right circular cone (Taylor 1959, p. 403).

<sup>3</sup> For ellipse and hyperbola only. The center for parabola is not defined.

TABLE 1. Parameters of the cases illustrated in section 3.

Case	$u_0$ (m s <sup>-1</sup> )	$v_0$ (m s <sup>-1</sup> )	$u_x$ (s <sup>-1</sup> )	$u_y$ (s <sup>-1</sup> )	$v_x$ (s <sup>-1</sup> )	$v_y$ (s <sup>-1</sup> )	$u_{xx}$ (m <sup>-1</sup> s <sup>-1</sup> )
A	10	10	0	0	0	0	0
B	0	0	$2 \times 10^{-4}$	0	0	$1 \times 10^{-4}$	0
C	0	0	$2 \times 10^{-4}$	0	0	$-1 \times 10^{-4}$	0
D	0	0	0	$1 \times 10^{-4}$	$1 \times 10^{-4}$	0	0
BD	0	0	$2 \times 10^{-4}$	$1 \times 10^{-4}$	$1 \times 10^{-4}$	$1 \times 10^{-4}$	0
CD	0	0	$2 \times 10^{-4}$	$1 \times 10^{-4}$	$1 \times 10^{-4}$	$-1 \times 10^{-4}$	0
AB	10	10	$2 \times 10^{-4}$	0	0	$1 \times 10^{-4}$	0
AC	10	10	$2 \times 10^{-4}$	0	0	$-1 \times 10^{-4}$	0
AD	10	10	0	$1 \times 10^{-4}$	$1 \times 10^{-4}$	0	0
ABD	10	10	$2 \times 10^{-4}$	$1 \times 10^{-4}$	$1 \times 10^{-4}$	$1 \times 10^{-4}$	0
ACD	10	10	$2 \times 10^{-4}$	$1 \times 10^{-4}$	$1 \times 10^{-4}$	$-1 \times 10^{-4}$	0
E1	0	0	0	0	0	0	$3 \times 10^{-7}$
E2	0	0	0	0	0	0	$3 \times 10^{-6}$
ABDE1	10	10	$2 \times 10^{-4}$	$1 \times 10^{-4}$	$1 \times 10^{-4}$	$1 \times 10^{-4}$	$3 \times 10^{-7}$
ABDE2	10	10	$2 \times 10^{-4}$	$1 \times 10^{-4}$	$1 \times 10^{-4}$	$1 \times 10^{-4}$	$3 \times 10^{-6}$

$$A(x - x_0)^2 + C(y - y_0)^2 = F \quad (9)$$

in the rotated coordinate system. It can be shown that (e.g., Korn and Korn 1961, 39–41)

$$u_x + v_y = A + C. \quad (10)$$

It can be concluded that the existence of shearing deformation ( $u_y + v_x \neq 0$ ) rotates the major axes of the conic sections of the  $rV_d$  pattern at an acute angle from the  $x$  and the  $y$  axes. The amount of rotation is a function of the stretching deformation and shearing deformation. While the resultant deformation (defined as the square root of the sum of the square of shearing and stretching deformation; Bluestein 1992, p. 100) is invariant, the shearing or stretching deformation is a property that is dependent on the coordinate system and can be made to disappear by selecting a proper coordinate system (e.g., axis of dilatation; Bluestein 1992, p. 99). This property of deformation is clearly illustrated using Eqs. (5), (8), and (9) while the total divergence/convergence is invariant according to Eq. (10).

It has been demonstrated mathematically that the presence of a linear, nonrotational wind field in DVAD framework yields a simple and concise bivariate quadratic polynomial in a Cartesian coordinate. The physical properties are intuitive to identify and interpret based on the straight-forward and well-known geometric relations between conic sections and quadratic equations. It is instrumental to examine basic patterns between  $V_d$  and  $rV_d$  on linear and low-order nonlinear wind fields and illustrate the fundamental differences between these two quantities.

### 3. Graphical illustration of $V_d$ and $rV_d$ on low-order polynomial flows

In this section, the  $V_d$  and  $rV_d$  patterns of basic flow fields from constant, linear to nonlinear winds are examined to illustrate the characteristics and differences of these two approaches. To the authors' knowledge, the  $V_d$  patterns of linear wind fields have not appeared in literature and textbooks. The parameters of those cases illustrated in this section are summarized in Table 1, and descriptive names are given in Table 2.

#### a. Constant flow

When the velocity field is a constant [i.e.,  $u(x, y) = C_1$ ,  $v(x, y) = C_2$ , and  $\mathbf{V} = C_1\mathbf{i} + C_2\mathbf{j}$ ], Eq. (4) becomes

$$rV_d = u(x, y)x + v(x, y)y = C_1x + C_2y, \quad (11)$$

which represents a set of parallel lines as illustrated in Jou et al. (2008). Then Eq. (2) reduces to

$$\nabla(rV_d) = u(x, y)\mathbf{i} + v(x, y)\mathbf{j} = C_1\mathbf{i} + C_2\mathbf{j}. \quad (12)$$

The same result can be directly deduced from Eq. (2). An example of a uniform southwesterly wind ( $u_0 = v_0 = 10 \text{ m s}^{-1}$ , case A) is illustrated in Fig. 2a1. The corresponding  $V_d$  holds a diverging (starburst) pattern centered at the radar (Fig. 2a2) while the  $rV_d$  pattern possesses a set of parallel lines oriented from northwest to southeast (Fig. 2a3), perpendicular to the prescribed uniform southwesterly wind (Fig. 2a1). Note that the wind direction is pointing from negative to positive contours according to Eq. (12). Although experienced radar scientists can identify the wind direction and speed from Fig. 2a2, the  $rV_d$  pattern is clearly simpler than the traditional  $V_d$  display.

TABLE 2. Descriptive names for each case listed in Table 1.

Case	Descriptive name
A	Constant wind
B	Zero shearing deformation flow ( $u_x v_y > 0$ )
C	Zero shearing deformation flow ( $u_x v_y < 0$ )
D	Pure shearing deformation flow
BD	Mixed divergence ( $u_x v_y > 0$ ) and shearing deformation flow
CD	Mixed divergence ( $u_x v_y < 0$ ) and shearing deformation flow
AB	Zero shearing deformation flow ( $u_x v_y > 0$ ) with constant wind
AC	Zero shearing deformation flow ( $u_x v_y < 0$ ) with constant wind
AD	Pure shearing deformation flow with constant wind
ABD	Mixed divergence ( $u_x v_y > 0$ ) and shearing deformation flow with constant wind
ACD	Mixed divergence ( $u_x v_y < 0$ ) and shearing deformation flow with constant wind
E1	Weak second-order nonlinear term
E2	Strong second-order nonlinear term
ABDE1	Mixed divergence ( $u_x v_y > 0$ ), shearing deformation flow with constant wind and weak nonlinear flow
ABDE2	Mixed divergence ( $u_x v_y < 0$ ), shearing deformation flow with constant wind and strong nonlinear flow

### b. Linear wind fields

In this subsection, it is shown that the linear wind fields can be represented by three basic quadratic curves. It is noted that shearing deformation is coordinate dependent (section 2c), all patterns illustrated in this subsection can be obtained by rotating the zero shearing deformation flow. The amount of rotation in the mathematic coordinate system of a given DVAD pattern indicates the relative magnitude of shearing deformation. Therefore, the zero shearing deformation flow is discussed as a building block in this subsection.

#### 1) ZERO SHEARING DEFORMATION FLOW ( $u_y + v_x = 0$ )

When  $u_y + v_x = 0$ , the corresponding  $rV_d$  patterns can be one of three nondegenerate quadratic curves, ellipse, hyperbola, and straight lines (a special case of parabola) depending on the sign and magnitude of  $u_x$  and  $v_y$ . When  $u_x$  and  $v_y$  are both positive (e.g.,  $u_x = 2v_y = 2 \times 10^{-4} \text{ s}^{-1}$ , case B1), the wind vectors are diverging from the singular point at the radar (Fig. 2b1). The corresponding  $rV_d$  patterns (Fig. 2b3) are concentric ellipses with all positive contours according to Eq. (5). In this example, the  $u$  gradient along the  $x$  axis is twice the  $v$  gradient along the  $y$  axis, so the major (minor) axis of the ellipse is along the  $y$  axis ( $x$  axis). Note that the  $V_d$  pattern (Fig. 2b2) appears elliptical but it cannot be shown mathematically as in  $rV_d$ . Therefore, it will be

referred to as ellipselike curves hereafter. When  $u_x$  and  $v_y$  are both negative ( $u_x < 0$  and  $v_y < 0$ ;  $u_x = 2v_y = -2 \times 10^{-4} \text{ s}^{-1}$ ), the wind vectors in Fig. 2b1 are reversed in direction (i.e., pointing toward the radar at the origin) and the patterns remain the same as a set of ellipses but the contour values in Figs. 2b2 and 2b3 are all negative (not shown). Note that the major axis of the ellipse is aligned with either the  $y$  ( $|u_x| > |v_y|$ ) or  $x$  ( $|u_x| < |v_y|$ ) axis. If  $u_x = v_y$ , both  $V_d$  and  $rV_d$  contours of the aforementioned wind fields are concentric circles (scaled differently) with positive (negative) contours representing a pure diverging (converging) flow (not shown).

When  $u_x$  and  $v_y$  are opposite signs (e.g.,  $u_x v_y < 0$ ,  $u_x = -2v_y = 2 \times 10^{-4} \text{ s}^{-1}$ , case C), the corresponding vector field is illustrated in Fig. 2c1 while  $V_d$  and  $rV_d$  patterns are a set of hyperbola-like curves and hyperbola (Figs. 2c2 and 2c3). Note that  $u_x > 0$  ( $v_y > 0$ ) represents a set of “east–west (north–south) opening hyperbola” with positive (negative)  $V_d$  and  $rV_d$  contours along the “opening” of the hyperbola while  $u_x < 0$  or  $v_y < 0$  represents conjugate hyperbolas (not shown).

If either  $u_x$  or  $v_y$  vanishes in the zero shearing deformation flow, the resulting  $rV_d$  pattern is a set of parallel lines (i.e., a special case of parabola when  $\delta = 0$ ). When  $u_x = 0$  ( $v = 0$ ), the lines parallel the  $x$  ( $y$ ) axis (not shown). Note that in zero shearing deformation flow cases, the major and minor axes are always aligned along either the  $x$  or the  $y$  axis.

#### 2) PURE SHEARING DEFORMATION FLOW ( $u_x = v_y = 0$ AND $u_y + v_x \neq 0$ )

When  $u_x = v_y = 0$  and  $u_y + v_x \neq 0$ , the  $rV_d$  pattern possesses a set of rectangular hyperbola with horizontal ( $x$  axis) and vertical ( $y$  axis) asymptotes and  $V_d$  possesses a set of hyperbola-like curves similar to  $rV_d$ . For example, the wind vectors of shearing deformation (e.g.,  $u_y + v_x > 0$ ,  $u_y = v_x = 10^{-4} \text{ s}^{-1}$ ,  $u_x = v_y = 0$ , case D) and the corresponding  $V_d$  and  $rV_d$  patterns are illustrated in Figs. 2d1, 2d2, and 2d3, respectively. Note that the major axes of the rectangular hyperbola or the hyperbola-like curves now are rotated  $45^\circ$  from either  $x$  or  $y$  axis compared to the zero shearing deformation flow cases. When  $u_y + v_x < 0$ , the  $V_d$  and  $rV_d$  patterns are conjugate of the pattern illustrated in Figs. 2d2 and 2d3 (not shown).

Here, the rectangular hyperbola depends only on the magnitude and the sign of  $u_y + v_x$ , not on the individual magnitude and/or signs of  $u_y$  and  $v_x$  as in the zero shearing deformation flow fields presented in section 3b(1). It is apparent that for a given  $u_y + v_x$  (i.e., shearing deformation), different combinations of  $u_y$  and  $v_x$  yield the same  $V_d$  and  $rV_d$  patterns, respectively. As a result, it is not possible to separate  $u_y$  and  $v_x$  for a given wind field

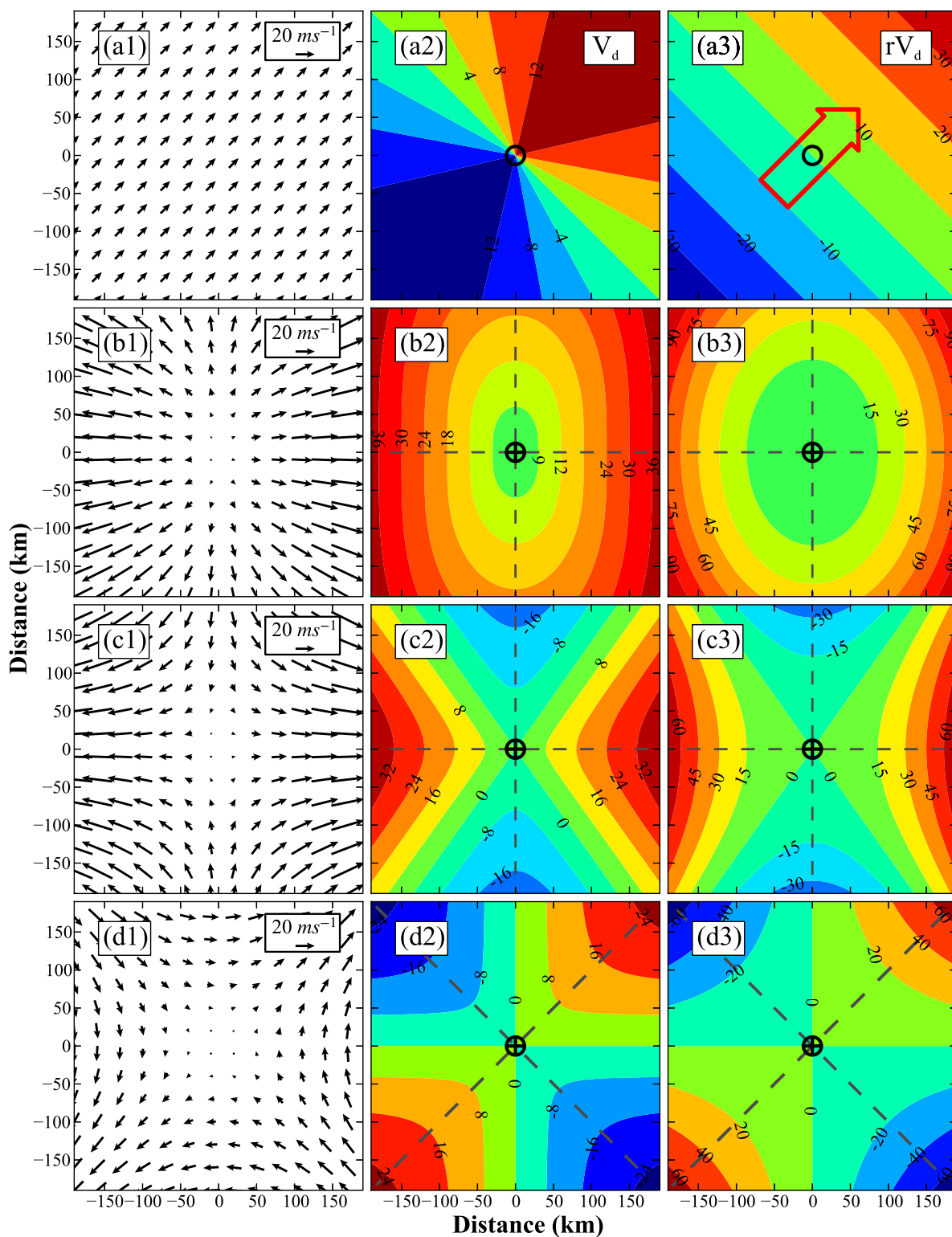


FIG. 2. Four basic linear flow fields: (a1)  $u_0 = 10.0$ ,  $u_x = 0$ ,  $u_y = 0$ ;  $v_0 = 10.0$ ,  $v_x = 0$ ,  $v_y = 0$ ; (b1)  $u_0 = 0$ ,  $u_x = 2 \times 10^{-4}$ ,  $u_y = 0$ ;  $v_0 = 0$ ,  $v_x = 0$ ,  $v_y = 1 \times 10^{-4}$ ; (c1)  $u_0 = 0$ ,  $u_x = 2 \times 10^{-4}$ ,  $u_y = 0$ ;  $v_0 = 0$ ,  $v_x = 0$ ,  $v_y = -1 \times 10^{-4}$ ; and (d1)  $u_0 = 0$ ,  $u_x = 0$ ,  $u_y = 1 \times 10^{-4}$ ;  $v_0 = 0$ ,  $v_x = 1 \times 10^{-4}$ ,  $v_y = 0$ . The corresponding Doppler velocities,  $V_d$ , sampled by a radar at (0, 0) are shown in (a2)–(d2). The corresponding DVAD patterns,  $rV_d$ , are shown in (a3)–(d3). The unit for the velocity is  $\text{m s}^{-1}$  and the unit for the first-order derivative is  $\text{s}^{-1}$ . The circle (○) and plus (+) represent the radar location and the center for the prescribed flow field, respectively. The units of  $V_d$  and  $rV_d$  are  $\text{m s}^{-1}$  and  $\text{m}^2 \text{s}^{-1}$ , respectively.



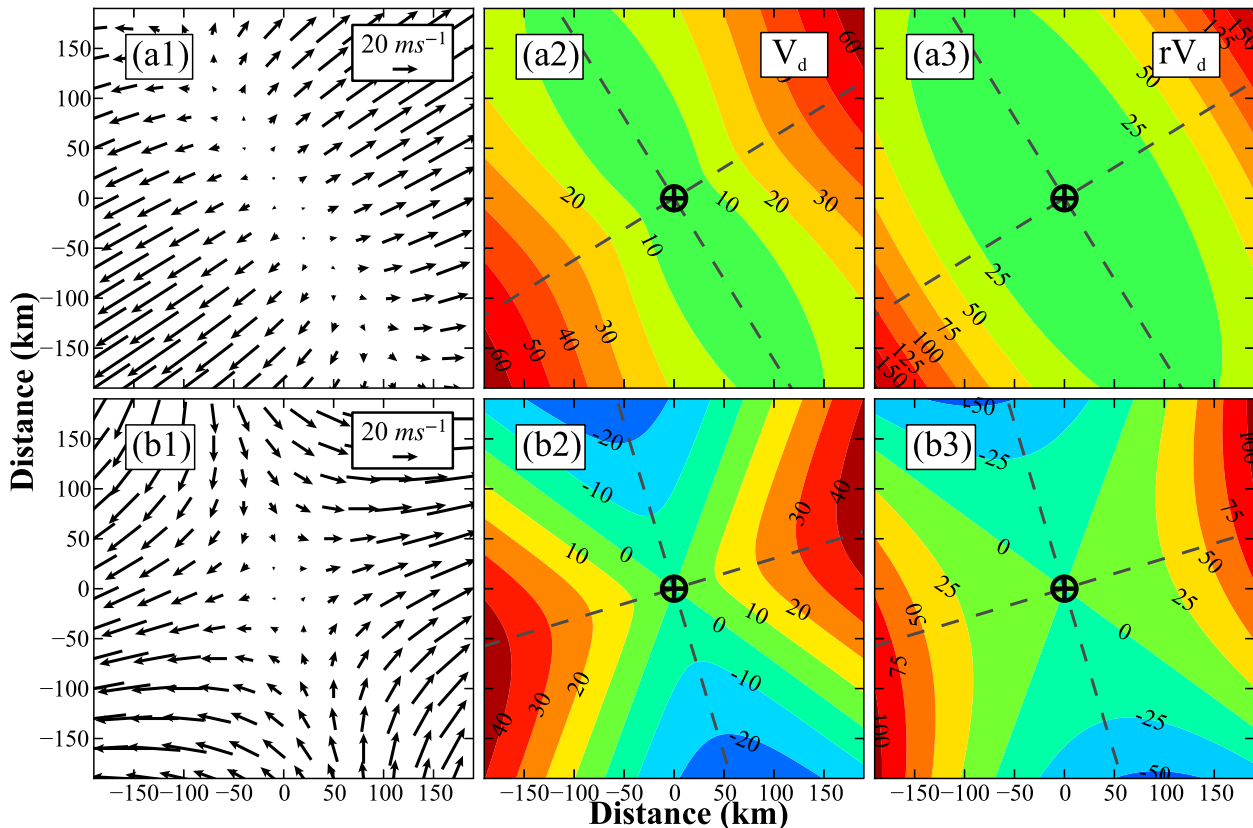


FIG. 3. As in Fig. 2, but for two flow fields including shearing deformation. (a1)  $u_0 = 0, u_x = 2 \times 10^{-4}, u_y = 1 \times 10^{-4}; v_0 = 0, v_x = 1 \times 10^{-4}, v_y = 1 \times 10^{-4}$ ; and (b1)  $u_0 = 0, u_x = 2 \times 10^{-4}, u_y = 1 \times 10^{-4}; v_0 = 0, v_x = 1 \times 10^{-4}, v_y = -1 \times 10^{-4}$ . The unit for the velocity is  $\text{m s}^{-1}$  and the unit for the first-order derivative is  $\text{s}^{-1}$ . The circle (O) and plus (+) represent the radar location and the center for the prescribed flow field, respectively. The units of  $V_d$  and  $rV_d$  are  $\text{m s}^{-1}$  and  $\text{m}^2 \text{s}^{-1}$ , respectively.

so unambiguously deducing vorticity is not possible. Hence, the full linear wind field cannot be retrieved from an observed  $rV_d$  pattern even though  $u_x$  and  $v_y$  can be uniquely distinguished as illustrated in subsection 3b(1). The result is consistent with the traditional  $V_d$ -based VAD formulation where the divergence ( $u_x + v_y$ ), stretching deformation ( $u_x - v_y$ ), and shearing deformation ( $u_y + v_x$ ) can be deduced, but vorticity ( $u_y - v_x$ ) remains elusive so the full wind field cannot be completely recovered. Therefore, a simple coordinate transformation from  $V_d$  (VAD) to  $rV_d$  (DVAD) simplifies the interpretation of the observed flow pattern but does not resolve new terms (i.e., provides new information).

### 3) MIXED LINEAR WIND FIELDS

In sections 3b(1) and 3b(2), the  $rV_d$  properties and graphical characteristics for polynomials of several simple cases were illustrated. These aforementioned basic  $rV_d$  patterns form the four basic building blocks (Figs. 2a–d) for interpreting other more complicated linear flow fields [i.e., any combinations of  $u_x, u_y + v_x$ , and  $v_y$  in Eq. (11)]. Based on Eq. (5), the combined  $rV_d$

pattern (ellipse, parabola, or hyperbola) is determined by the sign of  $\delta$  (i.e., the relative magnitude between shearing deformation, stretching deformation, and divergence). The following two examples illustrate the flow fields by combining zero and pure shearing deformation flows using those “building blocks.”

The first flow field (Fig. 3a1, case BD) is constructed by superimposing the zero shearing deformation flow (Fig. 2b1,  $u_x = 2v_y = 2 \times 10^{-4} \text{ s}^{-1}$ , case B) and the pure shearing deformation flow (Fig. 2d1,  $u_y = v_x = 10^{-4} \text{ s}^{-1}$ , case D) with the resulting  $V_d$  and  $rV_d$  patterns portrayed in Figs. 3a2 and 3a3. As predicted from Eqs. (5) and (8), the primary axes of the  $rV_d$  pattern illustrated in Fig. 3a3 rotates counterclockwise at an acute angle of  $31.7^\circ$ . The  $V_d$  pattern (Fig. 3a2) rotates the same magnitude as the  $rV_d$  pattern but the shape is a distorted ellipselike curve. The  $rV_d$  pattern is able to maintain the elliptical shape because the determinant  $\delta$  of Eq. (5) is less than zero in this case. If the flow matches the condition of  $u_y v_x = (u_y + v_x)^2/4$ , then the  $rV_d$  pattern is a set of straight lines (degenerate parabola with two identical real solutions, not shown). If the combination of zero and pure

shearing deformation flows makes  $\delta > 0$ , then the  $rV_d$  pattern becomes hyperbola (not shown).

The second flow field (Fig. 3b1, case CD) is constructed by superimposing the zero shearing deformation flow (Fig. 2c1,  $u_x = -2v_y = 2 \times 10^{-4} \text{ s}^{-1}$ , case C) and the pure shearing deformation flow (Fig. 2d1,  $u_y = v_x = 10^{-4} \text{ s}^{-1}$ , case D) with the resulting  $V_d$  and  $rV_d$  patterns portrayed in Figs. 3b2 and 3b3. This is the case where  $\delta$  is always greater than 0 when  $u_x$  and  $v_y$  have opposite signs. The characteristics of this set of  $V_d$  and  $rV_d$  patterns are very similar to the previous example in Fig. 3a with a set of hyperbola and hyperbola-like curves rotated  $16.8^\circ$  counterclockwise as predicted in Eq. (8). These examples demonstrate that the  $rV_d$  signature of pure linear wind field is cleaner than the  $V_d$  signature, an advantage of displaying Doppler velocity in the  $rV_d$  framework.

#### 4) SUPERIMPOSED LINEAR WIND FIELDS ON CONSTANT BACKGROUND WIND

The presence of background constant winds,  $u_0$  and  $v_0$ , geometrically translates the center of basic conic sections displayed in  $rV_d$  from  $(0, 0)$  to  $(x_0, y_0)$  where the magnitude and sign (i.e., direction) of the  $rV_d$  pattern translation depend on the characteristics of the background flow and the linear wind field specified in Eqs. (6) and (7). The following three examples illustrate the wind fields and the characteristics of  $V_d$  and  $rV_d$  of a linear wind field (portrayed in Figs. 2b–d) superimposed on a constant southwesterly background wind (Fig. 2a,  $u_0 = v_0 = 10 \text{ m s}^{-1}$ ).

Superimposing a zero shearing deformation flow when  $u_x v_y > 0$  ( $u_x > 0$  and  $v_y > 0$ ;  $u_x = 2v_y = 2 \times 10^{-4} \text{ s}^{-1}$ , Fig. 2b1, case B) onto the southeasterly background mean flow (Fig. 2a1, case A) shifts the flow center toward the southwest into the wind (Fig. 4a1, case AB) compared to Fig. 2b1. It has been illustrated before that the  $V_d$  and  $rV_d$  patterns of a zero shearing deformation flow are similar as concentric ellipse-like curves and ellipses (Figs. 2b2 and 2b3). However, when a constant background flow presents,  $rV_d$  patterns conserve their original concentric ellipses whose center is shifted to  $(-25 \text{ km}, -50 \text{ km})$  as predicted in Eqs. (6) and (7). Although the  $V_d$  display shifts to the same center as in  $rV_d$ ,<sup>4</sup> it has lost its original shape with only a hint of the ellipselike pattern remaining.

If the zero shearing deformation flow of  $u_x v_y < 0$  ( $u_x > 0$  and  $v_y < 0$ ;  $u_x = -2v_y = 2 \times 10^{-4} \text{ s}^{-1}$ , Fig. 2c1, case C) is superimposed onto the southwesterly background flow (Fig. 2a1, case A), the center of the wind pattern shifts to the northwest (Fig. 4b1, case AC). The  $rV_d$  pattern of this wind field (Fig. 4b3) remains a set of hyperbola with a new center at  $(-25 \text{ km}, 50 \text{ km})$  according to Eqs. (6) and (7). The corresponding  $V_d$  pattern (Fig. 4b2) is a set of distorted hyperbola-like curves.

When the constant southwesterly wind (Fig. 2a1, case A) is superimposed on the pure shearing deformation field ( $u_y + v_x > 0$ ,  $u_y = v_x = 10^{-4} \text{ s}^{-1}$ ,  $u_x = v_y = 0$ , Fig. 2d1, case D) the  $rV_d$  pattern maintains its hyperbola characteristics (Fig. 4c3, case AD) and shifts to a new center at  $(-50 \text{ km}, -50 \text{ km})$  according to Eqs. (6) and (7) while the  $V_d$  display is a set of distorted hyperbola-like curves (Fig. 4c2).

The following two examples illustrate the mixed linear wind fields (Fig. 3a1, case BC and Fig. 3b1, case BD) superimposed onto the constant background flow (Fig. 2a1). In the resulting wind fields (Fig. 5a1, case ABD, and Fig. 5b1, case ACD), the general characteristics of the  $V_d$  (Figs. 5a2 and 5b2) and  $rV_d$  patterns (Figs. 5a3 and 5b3) are very similar to those shown in simple linear wind fields (Figs. 4a–c) where the basic patterns of the  $rV_d$  (Figs. 5a3–5b3) are conserved with a translation while distortion in the  $V_d$  patterns (Figs. 5a2–5b2) is apparent. The centers in  $rV_d$  patterns were shifted to  $(0 \text{ km}, -50 \text{ km})$  and  $(-33.3 \text{ km}, 16.7 \text{ km})$  according to Eqs. (6) and (7), respectively. Note that in all five cases above, the zero  $V_d$  and  $rV_d$  contours are invariant according to the definition, and not affected by the variable transformation. Also one of the zero contours always passes through the radar at  $(0, 0)$  by definition.

Recall that the signatures of  $V_d$  and  $rV_d$  without the constant background flow are quite similar. From the above examples, there is a clear advantage of displaying the Doppler velocity in  $rV_d$  rather than  $V_d$  for interpretation and operational purposes because  $rV_d$  patterns are conserved in the presence of a constant background flow and the flow characteristics can be more easily deduced than with the conventional  $V_d$  display.

#### c. Nonlinear wind fields

The nonlinear wind fields discussed below are constructed by including the second order derivatives in the velocity fields as shown in Eq. (4). The second-order nonlinear wind field therefore possesses a cubic polynomial in the  $rV_d$  framework. The graphical expression of a cubic polynomial is complicated and the resulting  $rV_d$  patterns are not as straightforward to recognize as those of the quadratic equation, except for a few simple flow patterns. It can be seen, just like the quadratic

<sup>4</sup> By definition, both  $rV_d$  and  $V_d$  displays would shift to the same new origin when a constant background wind presents. The new origin is the point where the wind vanishes by superimposing the background wind and the specified linear wind field.

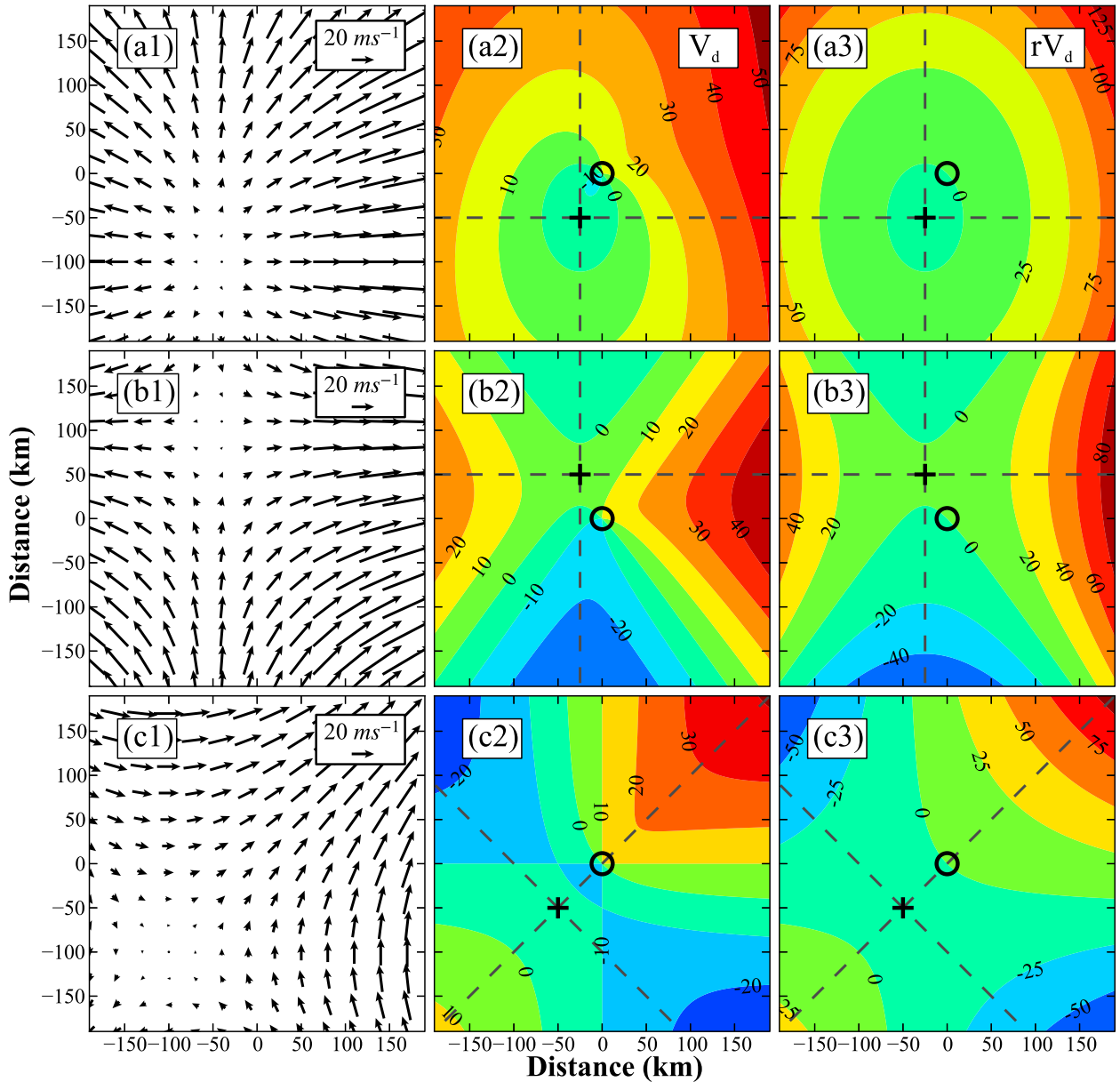


FIG. 4. As in Fig. 2, but for flow fields including translation. (a1)  $u_0 = 10, u_x = 2 \times 10^{-4}, u_y = 0; v_0 = 10, v_x = 0, v_y = 1 \times 10^{-4}$ ; (b1)  $u_0 = 10, u_x = 2 \times 10^{-4}, u_y = 0; v_0 = 10, v_x = 0, v_y = -1 \times 10^{-4}$ ; and (c1)  $u_0 = 10, u_x = 0, u_y = 1 \times 10^{-4}; v_0 = 10, v_x = 1 \times 10^{-4}, v_y = 0$ . The unit for the velocity is  $\text{m s}^{-1}$  and the unit for the first-order derivative is  $\text{s}^{-1}$ . The circle (O) and plus (+) represent the radar location and the center for the prescribed flow field, respectively. The units of  $V_d$  and  $rV_d$  are  $\text{m s}^{-1}$  and  $\text{m}^2 \text{s}^{-1}$ , respectively.

equation, that several second-order derivatives are grouped together and cannot be individually determined unambiguously.

Examples of both weak and strong simple nonlinear wind fields (with only  $u_{xx} \neq 0$  in the nonlinear terms, case E1, not shown) superimposed onto the same linear wind field illustrated in Fig. 5a1 (case ABD) are portrayed in Fig. 6. For the case of a weak nonlinear wind field (Fig. 6a1, case ABDE1), the resulting  $V_d$  (Fig. 6a2) and  $rV_d$

patterns (Fig. 6a3) are still similar to that of the linear case (Figs. 5a2 and 5a3). For the case of a strong nonlinear wind field (10 times the weak nonlinear case, Fig. 6b1, case E2, not shown), the  $V_d$  and  $rV_d$  patterns (Figs. 6b2 and 6c2, case ABDE2) possess hardly any signs of the original linear patterns in  $V_d$  and  $rV_d$  (Figs. 5a2 and 5a3). The general characteristics of these linear wind fields mixed with other second-order nonlinear wind fields (not shown) are similar to the examples shown in Fig. 6.

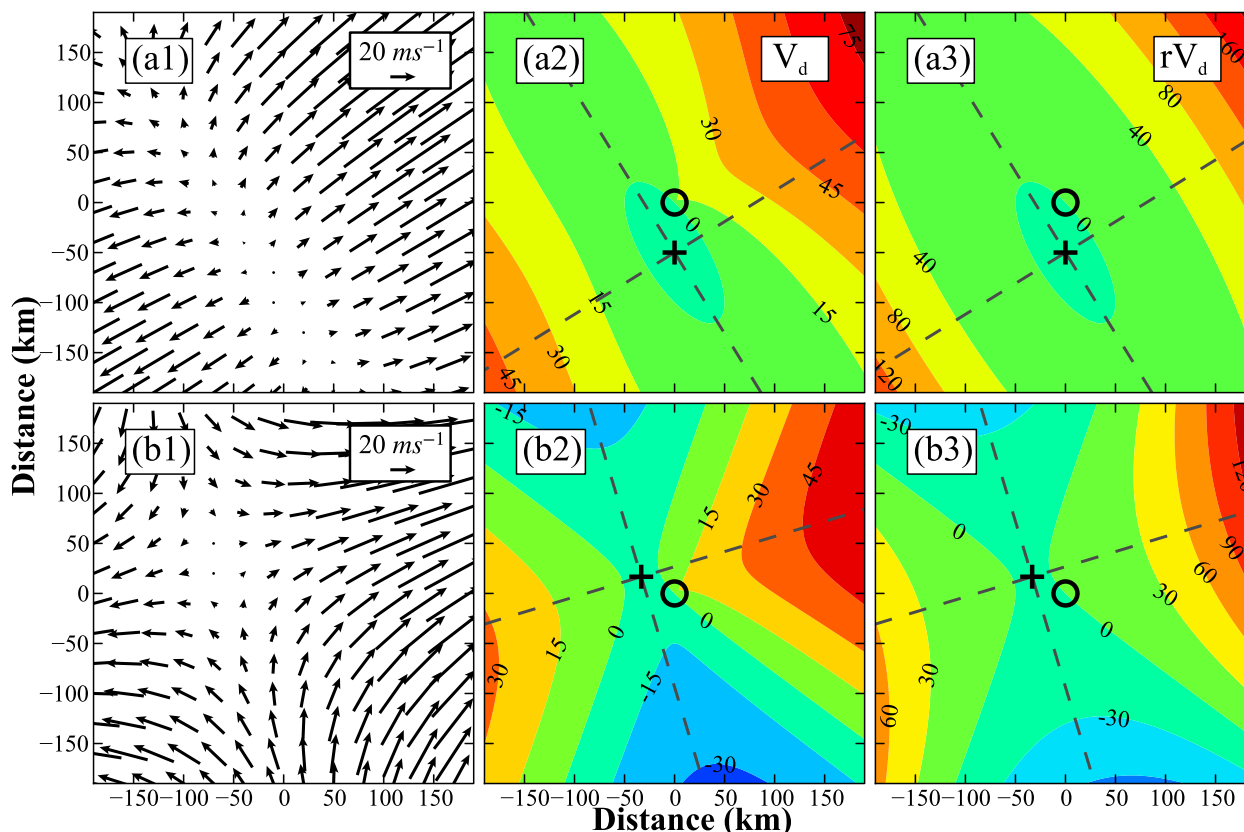


FIG. 5. As in Fig. 2, but for flow fields including mean wind, diverging/converging, and shearing deformation. (a1)  $u_0 = 10$ ,  $u_x = 2 \times 10^{-4}$ ,  $u_y = 1 \times 10^{-4}$ ,  $v_0 = 10$ ,  $v_x = 1 \times 10^{-4}$ ,  $v_y = 1 \times 10^{-4}$ ; and (b1)  $u_0 = 10$ ,  $u_x = 2 \times 10^{-4}$ ,  $u_y = 1 \times 10^{-4}$ ,  $v_0 = 10$ ,  $v_x = 1 \times 10^{-4}$ ,  $v_y = -1 \times 10^{-4}$ . The unit for the velocity is  $\text{m s}^{-1}$  and the unit for the first-order derivative is  $\text{s}^{-1}$ . The circle (○) and plus (+) represent the radar location and the center for the prescribed flow field, respectively. The units of  $V_d$  and  $rV_d$  are  $\text{m s}^{-1}$ , and  $\text{m}^2 \text{s}^{-1}$ , respectively.

The Taylor series expansion can be conducted to third and higher orders, but the graphical characteristics possess only limited applications in practice. Therefore, no further graphical examples of the higher-order nonlinear wind fields will be provided and discussed. Nevertheless, the  $rV_d$  display can be used to determine the degree of linearity of the underlying wind field, a valuable tool to assess the validity of the properties deduced by the VAD for both research and operational purposes.

#### 4. Retrieval of quantitative flow information

It has been illustrated in previous sections that linear and nonlinear wind fields can be represented as polynomials in the DVAD framework whose coefficients link to the flow characteristics and/or their combinations. It is also clear that for a given  $rV_d$  pattern, only a subset of those flow characteristics, not the full wind field, can be estimated qualitatively. Quantitative information of the wind field (i.e., coefficients of the polynomial) can be obtained by 1) the least squares method or 2) the derivative method. Both methods can be performed on nonlinear

wind fields. In this section, we will only illustrate the DVAD analysis using a linear wind field (mixture of a background mean wind, diverging flow and deformation flow, case ABD). To test the sensitivity of the two methods to random noise in the observations, a  $2 \text{ m s}^{-1}$  random noise is added to the analytic wind field (Fig. 7a1) that represents  $\sim 10\%$  uncertainty. The corresponding  $V_d$  and  $rV_d$  displays are respectively illustrated in Figs. 7a2,a3 that resemble their perfect fields in Figs. 5a2 and 5a3.

The least squares fit method is a standard approach and has been widely used in many single-Doppler wind retrieval algorithms, such as VAD (e.g., Browning and Wexler 1968), VVP (e.g., Waldteufel and Corbin 1979), and VTD (e.g., Lee et al. 1994). Therefore, the details will not be repeated here. The derivative method is described in detail in this section.

The quantitative DVAD analysis can also be performed via successive differentiation of Eq. (5) with respect to  $x$  and  $y$  to deduce the coefficients. Each differentiation will eliminate the lowest-order terms in the previous set of equations and eventually the highest-order terms will emerge when the lower-order derivatives vanish. This

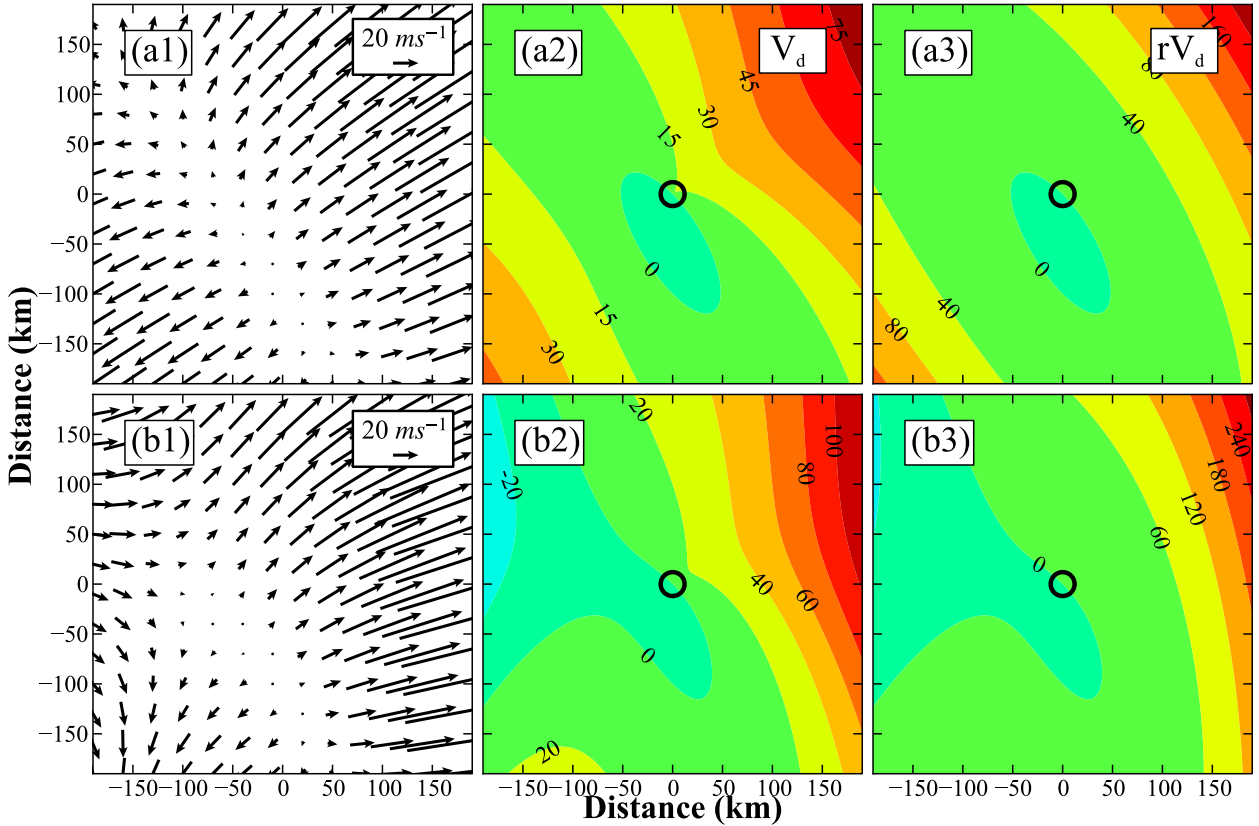


FIG. 6. As in Fig. 2, but for flow fields including linear and nonlinear (weak upper, strong bottom) terms. (a1)  $u_0 = 10$ ,  $u_x = 2 \times 10^{-4}$ ,  $u_y = 1 \times 10^{-4}$ ;  $v_0 = 10$ ,  $v_x = 1 \times 10^{-4}$ ,  $v_y = 1 \times 10^{-4}$ ,  $u_{xx} = 3 \times 10^{-7}$ ; and (b1)  $u_0 = 10$ ,  $u_x = 2 \times 10^{-4}$ ,  $u_y = 1 \times 10^{-4}$ ;  $v_0 = 10$ ,  $v_x = 1 \times 10^{-4}$ ,  $v_y = 1 \times 10^{-4}$ ,  $u_{xx} = 3 \times 10^{-6}$ . The unit for the velocity is  $\text{m s}^{-1}$ , the unit for the first-order derivative is  $\text{s}^{-1}$ , and the unit for the second-order derivative is  $\text{m}^{-1} \text{s}^{-1}$ . The circle (O) represents the radar location. The units of  $V_d$  and  $rV_d$  are  $\text{m s}^{-1}$  and  $\text{m}^2 \text{s}^{-1}$ , respectively.

property is another advantage of DVAD over those  $V_d$ -based single-Doppler wind retrieval algorithms operating in the polar coordinate system.

This property can be illustrated by using a bivariate quadratic polynomial in Eq. (5). By taking the derivative of Eq. (5) with respect to  $x$  and  $y$ , we obtain the following:

$$\frac{\partial(rV_d)}{\partial x} = 2u_x x + (u_y + v_x)y + u_0, \quad (13)$$

$$\frac{\partial(rV_d)}{\partial y} = 2v_y y + (u_y + v_x)x + v_0. \quad (14)$$

Evaluating Eqs. (13) and (14) at the origin ( $x = y = 0$ ),<sup>5</sup> we obtain  $u_0$  and  $v_0$  as shown in Eq. (2). By taking the

derivative of Eqs. (13) and (14) with respect to  $x$  and  $y$ , we obtain three independent equations:

$$\frac{\partial^2(rV_d)}{\partial x^2} = 2u_x, \quad (15)$$

$$\frac{\partial^2(rV_d)}{\partial x \partial y} = u_y + v_x, \quad (16)$$

$$\frac{\partial^2(rV_d)}{\partial y^2} = 2v_y. \quad (17)$$

In this linear wind field, Eqs. (15)–(17) should be constant by definition. Hence  $u_x$ ,  $(u_y + v_x)$  and  $v_y$  can be obtained. Therefore,  $u_0$  and  $v_0$  can be obtained within the entire domain by evaluating Eqs. (13) and (14) using Eqs. (15)–(17). If the wind field is nonlinear, then Eqs. (15)–(17) will not be constant.

Coefficients of a higher-order polynomial can be obtained theoretically in a similar manner. While taking derivatives of a field is straightforward compared with a 2D least squares curve fit, the derivative method

<sup>5</sup> It is understood that radar location is a singularity in  $V_d$  and the radar data at close range are highly likely contaminated by ground clutter. However, since  $rV_d$  is a scalar,  $rV_d$  at the radar can be obtained by 2D filling/interpolating from nearby valid  $rV_d$ .

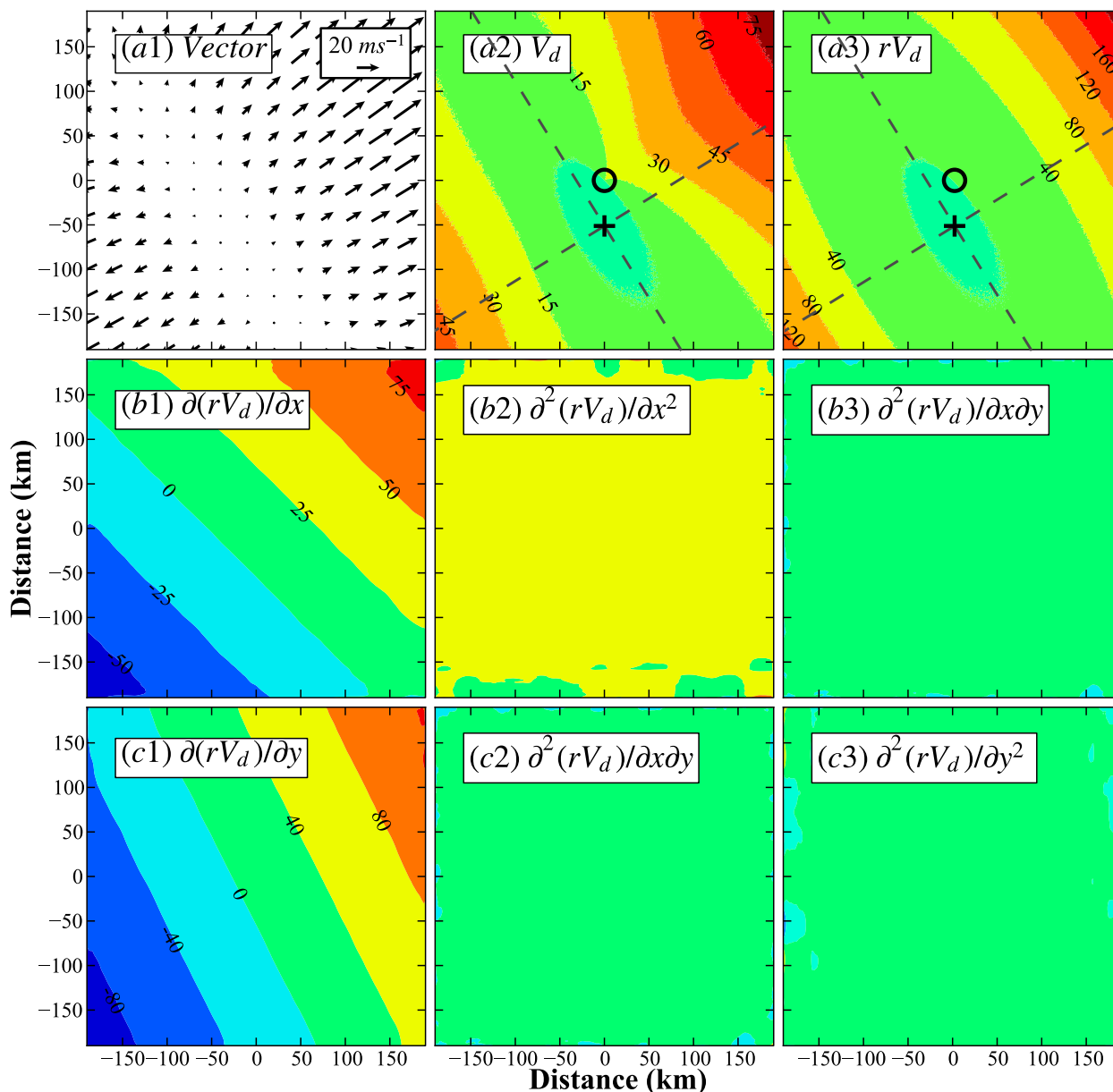


FIG. 7. Results of derivative method on a linear wind field (wind field parameters are listed in the following table, with  $2 \text{ m s}^{-1}$  of noise). (a1)  $\mathbf{u}, \mathbf{v}$  vector; (a2)  $V_d$  contour; (a3)  $rV_d$  contour; (b1)  $\partial(rV_d)/\partial x$ ; (b2)  $\partial^2(rV_d)/\partial x^2$ ; (b3)  $\partial^2(rV_d)/\partial x\partial y$ ; (c1)  $\partial(rV_d)/\partial y$ ; (c2)  $\partial^2(rV_d)/\partial y\partial x$ ; and (c3)  $\partial^2(rV_d)/\partial y^2$ . The circle ( $\circ$ ) and plus (+) represent the radar location and the center for the prescribed flow field, respectively. The units of  $V_d$  and  $rV_d$  are  $\text{m s}^{-1}$  and  $\text{m}^2 \text{ s}^{-1}$ , respectively.

amplifies local noise with each differentiation. Therefore, when applying the derivative method to real data, the 2D field of  $rV_d$  and their subsequent derivatives need to be filtered/smoothed before each differentiation.

The results of quantitative DVAD analysis of the prescribed linear wind field (case ABD) using the least squares fit and the derivative methods are illustrated in Table 3. It can be concluded from Table 3 that both approaches yield almost identical results. The retrieved

$u_0$  and  $v_0$  are within 10% of the specified analytical field while the three linear terms are nearly identical to the true values. The least squares fit method is not sensitive to the random noise. The graphical representation of the deduction in Eqs. (13)–(17) is shown in Figs. 7b1–b3, c1–c3. According to Eqs. (13)–(14), for a linear wind field, the first derivative of  $rV_d$  with respect to  $x$  and  $y$  should be two sets of parallel lines as illustrated in Figs. 7b1, c1 while the second derivative [Eqs. (15)–(17)] should be

TABLE 3. The true coefficients of this linear wind field and the retrieved coefficient from two different approaches.

	$u_0(\text{m s}^{-1})$	$v_0(\text{m s}^{-1})$	$u_x(\text{s}^{-1})$	$v_y(\text{s}^{-1})$	$u_y + v_x(\text{s}^{-1})$
True	10	8	0.1	0.1	0.02
Fitting	11	9	0.1	0.1	0.02
Derivative	11	8.9	0.095	0.106	0.02

constant as illustrated in Fig. 7. It is evident from Fig. 7 that the derivative method is still applicable when noise is presented in data, provided proper filtering is applied to the intermediate results.

### 5. Graphical interpretation of real wind fields using $rV_d$

The concept and mathematic framework of DVAD has been derived and illustrated using analytical wind fields on a constant altitude in previous sections. The application of DVAD to graphically interpret the real, near-surface, flow pattern from low elevation angle single-Doppler radar PPI<sup>6</sup> observations is portrayed by an example involving two mesoscale convective systems (MCSs). On 7 June 2003, a squall line approached southern Taiwan and was observed by an S-band Doppler radar (RCKT) operated by the Central Weather Bureau of Taiwan. The RCKT 0.5° reflectivity PPI overlaid with  $V_d$  and  $rV_d$  contours are illustrated in Figs. 8a and 8b, respectively. The target squall line is located ~100 km west of the RCKT, and another MCS was located ~50 km east of RCKT. Note the wedge between 300° and 30° azimuth was blocked by terrain in southern Taiwan.

An experienced radar meteorologist can identify a general southwesterly wind ahead of the squall line and a general westerly jet behind the squall line based on the distribution of  $V_d$  (Figs. 8a,c). The convergence along the southern part of the squall line is indicated by a weak Doppler velocity contour followed by stronger Doppler velocities behind the line. These flow characteristics are more intuitive in the  $rV_d$  display (Figs. 8b,d) where the general flow directions are indicated by the red arrows. Relatively uniform flow fields are represented by localized near parallel straight contours of  $rV_d$ , such as to the southeast of RCKT. For example, the southwesterly winds southwest of the RCKT turned into west-southwesterly winds to the east of the RCKT where the winds approached the back side of the MCS. The location of the squall line (i.e., high

reflectivity) is accompanied by curved  $rV_d$  contours, indicating a nonuniform wind shift across the squall line. The  $rV_d$  contours were also curved within that MCS but the curvature was not as steep as that within the squall line. This region of curved  $rV_d$  contours along the squall line is a region of convergence between northwesterly (behind the line) and southerly (ahead of the line).

### 6. Summary and future work

This paper presents the concept of the distance velocity–azimuth display (DVAD) methodology and basic applications of DVAD to linear and nonlinear wind fields on a constant altitude PPI plane. DVAD is an alternative approach to express and interpret single-Doppler velocities that use a nearly forgotten form of  $rV_d$ . The Doppler velocity  $V_d$  is a vector field in the radar-centric spherical coordinate that has been used by radar meteorologists in the past six decades. In contrast, the DVAD framework allows  $rV_d$  to be expressed in the form of a polynomial in a Cartesian coordinate system, linking  $rV_d$  directly to  $x$ ,  $y$ , and  $z$ , and the 3D velocities ( $u$ ,  $v$ , and  $w$ ). The gradient of  $rV_d$  is mathematically related to the true 3D wind vectors and their first-order derivatives at each grid point. Therefore,  $rV_d$  possesses a property similar to a type of velocity potential in fluid mechanics rather than a vector property possessed by  $V_d$ . Although  $rV_d$  has been introduced in Peace et al. (1969) and Gal-Chen (1982) on synthetic dual-Doppler radar applications and determining the optimal moving frame of reference, its advantages in simplifying Doppler velocity signatures, especially on linear wind fields, have not previously been explored.

The major merit of representing the single-Doppler radar velocity in the  $rV_d$  framework is its direct link to the well-known polynomial functions. A Taylor series expansion of a 3D wind field with respect to the radar site expressed in the  $rV_d$  framework corresponds to a polynomial with one order higher than the order of the prescribed wind field. This relationship is especially useful when the actual wind field is linear (or quasi linear). The resulting mathematic form of  $rV_d$  is a bivariate quadratic polynomial representing three conic sections: ellipse, parabola, and hyperbola, depending on the magnitudes and signs of those first-order derivative terms of the wind field.

When illustrated in 2D on a CAPPI, the  $rV_d$  patterns of zero shearing deformation flow can be either ellipse or hyperbola with primary axes aligned with the  $x$  or  $y$  axis while the  $rV_d$  patterns of pure shearing deformation flow form rectangular hyperbola with its primary axis rotating 45° from their diverging/converging flow

<sup>6</sup>The PPI data will need to be interpolated into CAPPI for interpretation of wind fields above the surface layer.



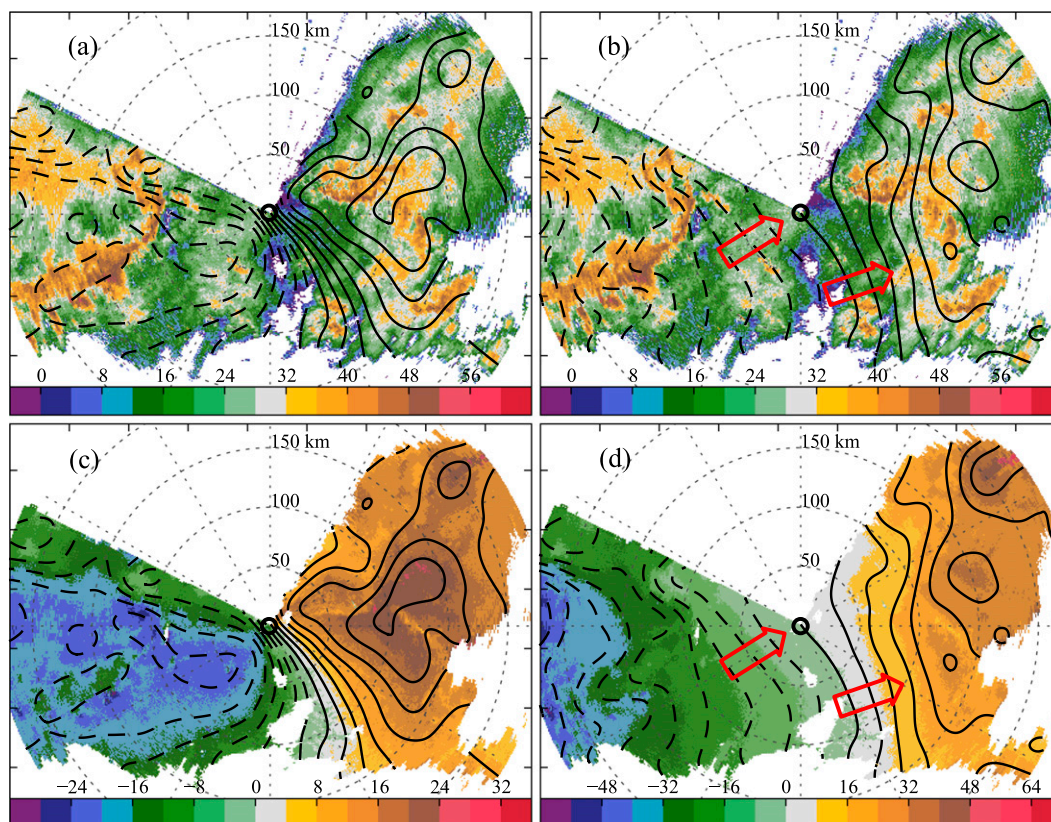


FIG. 8. The Doppler radar observations of a squall line approaching RCKT (at the origin indicated by a circle). (a) Reflectivity (dBZ) in color overlaid with Doppler velocity contours ( $\text{m s}^{-1}$ ), (b) reflectivity in color overlaid with  $rV_d$  contours ( $\times 100 \text{ m}^2 \text{ s}^{-1}$ ), (c) Doppler velocity in color and contours, and (d)  $rV_d$  in color and contours. The red arrows indicate wind directions estimated from the gradient of  $rV_d$ .

counterparts. The corresponding  $V_d$  display possesses a similar pattern as its  $rV_d$  counterpart. When mixing linear wind fields, the resulting  $rV_d$  patterns remain as one of the conic sections but rotate at an angle determined by the sign and magnitudes of these linear terms. However, the distortion is apparent in the corresponding  $V_d$  display. The presence of a constant background flow for the  $rV_d$  pattern of a linear wind field is equivalent to translating the center of the  $rV_d$  pattern from the radar to a new location determined by the background winds and the linear terms. In contrast, the corresponding  $V_d$  display loses its original shape. Although VAD and DVAD deduce the same information when the wind field is linear, in practice, it is feasible to graphically estimate the characteristics of the actual wind field from  $rV_d$  without performing a VAD analysis.

The quantitative DVAD analysis can be processed via either a 2D bivariate least squares fitting or a derivative method. The Cartesian-based DVAD analysis can be used to derive the information of linear wind fields by the same way as that of VAD and VVP, but a clear

advantage appears when dealing with data with asymmetric distribution and/or large sectors of missing data. The concise formula of DVAD also makes it straightforward to extend the method to analyze single-Doppler radar observations subject to nonlinearity.

For nonlinear wind fields, the differences between processing the same observed Doppler velocity field in VAD and in DVAD are significant because flow characteristics derived from the VAD Fourier coefficients are only valid under linear wind fields (Caya and Zawadzki 1992) while DVAD coefficients can be extended to include nonlinearity in a straightforward way. In comparison, the DVAD framework does not have this limitation where the mean wind can be deduced even for nonlinear wind fields, thus it is more accurate than those obtained from the VAD. Applying DVAD to the nonlinear wind field and examining the vertical wind profiles between DVAD and Caya and Zawadzki (1992) methodologies using analytical data and real cases are currently under way and will be documented in a future paper.



**Acknowledgments.** The authors thank Drs. Tammy Weckwerth and Scott Ellis, and Mr. John Tuttle for their helpful comments on the manuscript. The discussions with Dr. Michael Bell were instrumental. Comments from three anonymous reviewers greatly improved this manuscript. The second author is grateful for the support by the Graduate Student Visitor Program of the NCAR Advanced Study Program and the Earth Observing Laboratory during this research.

## REFERENCES

- Armijo, L., 1969: A theory for the determination of wind and precipitation velocities with Doppler radars. *J. Atmos. Sci.*, **26**, 570–573.
- Bluestein, H. B., 1992: *Synoptic-Dynamic Meteorology in Mid-latitudes*. Vol. 1. Oxford University Press, 431 pp.
- , and D. S. Hazen, 1989: Doppler radar analysis of a tropical cyclone over land: Hurricane Alicia (1983) in Oklahoma. *Mon. Wea. Rev.*, **117**, 2594–2611.
- , S. D. Hrebenach, and C.-F. Chang, 1994: Synthetic dual-Doppler analysis of mesoscale convective systems. *Mon. Wea. Rev.*, **122**, 2105–2124.
- Boccippio, D. J., 1995: A diagnostic analysis of the VVP single Doppler retrieval technique. *J. Atmos. Oceanic Technol.*, **12**, 230–248.
- Browning, K. A., and R. Wexler, 1968: The determination of kinematic properties of a wind field using Doppler radar. *J. Appl. Meteor.*, **7**, 105–113.
- Caya, D., and I. Zawadzki, 1992: VAD analysis of nonlinear wind field. *J. Atmos. Oceanic Technol.*, **9**, 575–587.
- Donaldson, R. J., Jr., 1970: Vortex signature recognition by a Doppler radar. *J. Appl. Meteor.*, **9**, 661–670.
- , 1991: A proposed technique for diagnosis by radar of hurricane structure. *J. Appl. Meteor.*, **30**, 1636–1645.
- Gal-Chen, T., 1982: Errors in fixed and moving frame of reference: Applications for conventional and Doppler radar analysis. *J. Atmos. Sci.*, **39**, 2279–2300.
- Jou, B. J.-D., W.-C. Lee, S.-P. Liu, and Y.-C. Kao, 2008: Generalized VTD (GVTD) retrieval of atmospheric vortex kinematic structure. Part I: Formulation and error analysis. *Mon. Wea. Rev.*, **136**, 995–1012.
- Korn, C. A., and T. M. Korn, 1961: *Mathematical Handbook for Scientists and Engineers*. McGraw-Hill Book Company, Inc., 943 pp.
- Koscielny, A. J., R. J. Doviak, and R. Rabin, 1982: Statistical considerations in the estimation of divergence from single-Doppler radar and application to prestorm boundary-layer observations. *J. Appl. Meteor.*, **21**, 197–210.
- Lee, W.-C., F. D. Marks, and R. E. Carbone, 1994: Velocity Track Display (VTD)—A technique to extract primary vortex circulation of a tropical cyclone in real time using single airborne Doppler radar data. *J. Atmos. Oceanic Technol.*, **11**, 337–356.
- , B. J.-D. Jou, P.-L. Chang, and S.-M. Deng, 1999: Tropical cyclone kinematic structure retrieved from single-Doppler radar observations. Part I: Interpretation of Doppler velocity patterns and the GBVTD technique. *Mon. Wea. Rev.*, **127**, 2419–2439.
- Lhermitte, R. M., and D. Atlas, 1961: Precipitation motion by pulse Doppler radar. Preprints, *Ninth Weather Radar Conf.*, Kansas City, KS, Amer. Meteor. Soc., 218–223.
- Matejka, T., and R. C. Srivastava, 1991: An improved version of the extended VAD analysis of single Doppler radar data. *J. Atmos. Oceanic Technol.*, **8**, 453–466.
- Peace, R. L., Jr., R. A. Brown, and H. G. Camnitz, 1969: Horizontal motion field observations with a single pulse Doppler radar. *J. Atmos. Sci.*, **26**, 1096–1103.
- Roux, F., and F. D. Marks, 1996: Extended velocity track display (EVTD): An improved processing method for Doppler radar observations of tropical cyclones. *J. Atmos. Oceanic Technol.*, **13**, 875–899.
- Taylor, A. E., 1959: *Calculus with Analytic Geometry*. Prentice-Hall, Inc., 762 pp.
- Waldteufel, P., and H. Corbin, 1979: On the analysis of single-Doppler radar data. *J. Appl. Meteor.*, **18**, 532–542.
- Wood, V. T., and R. A. Brown, 1992: Effects of radar proximity on single-Doppler velocity of axisymmetric rotation and divergence. *Mon. Wea. Rev.*, **120**, 2798–2807.